

Intricate Resonant Raman Response in Anisotropic ReS<sub>2</sub>

Amber McCreary,<sup>†,‡,§,¶</sup> Jeffrey R. Simpson,<sup>§,||</sup> Yuanxi Wang,<sup>†,Δ,¶</sup> Daniel Rhodes,<sup>‡,⊥</sup> Kazunori Fujisawa,<sup>†</sup> Luis Balicas,<sup>⊥,¶</sup> Madan Dubey,<sup>‡</sup> Vincent H. Crespi,<sup>†,‡,∇,Δ</sup> Mauricio Terrones,<sup>\*,†,‡,∇,¶</sup> and Angela R. Hight Walker<sup>\*,§,¶</sup>

<sup>†</sup>Department of Physics and Center for 2-Dimensional and Layered Materials, <sup>#</sup>Department of Materials Science & Engineering, <sup>Δ</sup>2-Dimensional Crystal Consortium, Materials Research Institute, <sup>∇</sup>Department of Chemistry, The Pennsylvania State University, University Park, Pennsylvania 16802, United States

<sup>‡</sup>Sensors & Electron Devices Directorate, U.S. Army Research Laboratory, Adelphi, Maryland 20783, United States

<sup>§</sup>Engineering Physics Division, Physical Measurement Laboratory, National Institute of Standards and Technology, Gaithersburg, Maryland 20899, United States

<sup>||</sup>Department of Physics, Astronomy, and Geosciences, Towson University, Towson, Maryland 21252, United States

<sup>⊥</sup>Department of Physics and National High Magnetic Field Lab, Florida State University, Tallahassee, Florida 32310, United States

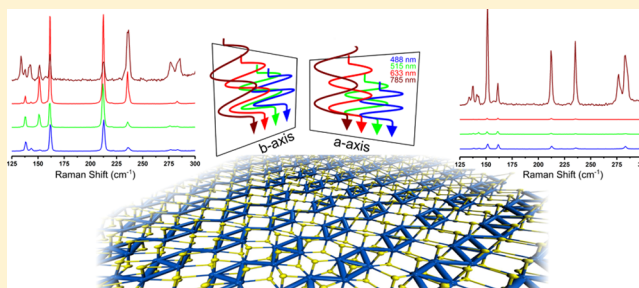
<sup>¶</sup>Institute of Carbon Science and Technology, Faculty of Engineering, Shinshu University, Nagano 380-8553, Japan

**S** Supporting Information

**ABSTRACT:** The strong in-plane anisotropy of rhenium disulfide (ReS<sub>2</sub>) offers an additional physical parameter that can be tuned for advanced applications such as logic circuits, thin-film polarizers, and polarization-sensitive photodetectors. ReS<sub>2</sub> also presents advantages for optoelectronics, as it is both a direct-gap semiconductor for few-layer thicknesses (unlike MoS<sub>2</sub> or WS<sub>2</sub>) and stable in air (unlike black phosphorus). Raman spectroscopy is one of the most powerful characterization techniques to nondestructively and sensitively probe the fundamental photophysics of a 2D material. Here, we perform a thorough study of the resonant Raman response of

the 18 first-order phonons in ReS<sub>2</sub> at various layer thicknesses and crystal orientations. Remarkably, we discover that, as opposed to a general increase in intensity of all of the Raman modes at excitonic transitions, each of the 18 modes behave *differently* relative to each other as a function of laser excitation, layer thickness, and orientation in a manner that highlights the importance of electron–phonon coupling in ReS<sub>2</sub>. In addition, we correct an unrecognized error in the calculation of the optical interference enhancement of the Raman signal of transition metal dichalcogenides on SiO<sub>2</sub>/Si substrates that has propagated through various reports. For ReS<sub>2</sub>, this correction is critical to properly assessing the resonant Raman behavior. We also implemented a perturbation approach to calculate frequency-dependent Raman intensities based on first-principles and demonstrate that, despite the neglect of excitonic effects, useful trends in the Raman intensities of monolayer and bulk ReS<sub>2</sub> at different laser energies can be accurately captured. Finally, the phonon dispersion calculated from first-principles is used to address the possible origins of unexplained peaks observed in the Raman spectra, such as infrared-active modes, defects, and second-order processes.

**KEYWORDS:** Rhenium disulfide, polarization, laser wavelength, resonant Raman, anisotropy, defects



Starting with the mechanical exfoliation of graphene in 2004,<sup>1</sup> there has been a plethora of research dedicated to two-dimensional (2D) materials due to their compelling physics and potential applications.<sup>2–5</sup> Although graphene displays remarkable physics,<sup>3</sup> its lack of a bandgap limits its use in many applications, such as field-effect transistors (FETs), solar cells, and optoelectronic devices. Thus, a new class of 2D materials, the transition metal dichalcogenides (TMDs), has risen in prominence due to the visible-range (1.3–2.0 eV) bandgaps of its semiconducting members.<sup>6,7</sup> A TMD monolayer is three atoms thick typically with an MX<sub>2</sub> formula unit, where M is a transition metal (e.g., Mo, W, Re, Sn) and X is a chalcogen (S, Se, or Te). Depending on M and X, these

materials can be semiconducting, metallic, or superconducting and may support charge density waves.<sup>4,8,9</sup>

ReS<sub>2</sub> is a semiconducting TMD that crystallizes in a distorted octahedral (1T') structure (Figure 1a) with reduced symmetry compared to the typical trigonal prismatic (2H) MoS<sub>2</sub> and WS<sub>2</sub>.<sup>10–13</sup> On the basis of recent experimental findings by Aslan et al., ReS<sub>2</sub> is deduced to be a direct gap semiconductor (~1.4–1.5 eV) for few-layer thicknesses.<sup>14</sup> For monolayer and bulk samples, the exact nature of the gap, i.e., direct or indirect,

**Received:** April 7, 2017

**Revised:** August 16, 2017

**Published:** August 18, 2017



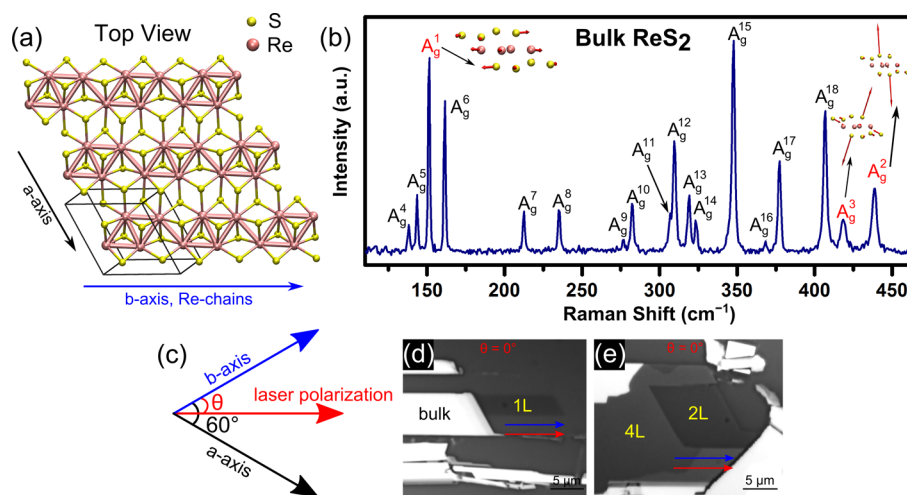


**Figure 1.** (a) Top view of the 1T' crystal structure of ReS<sub>2</sub>. The *b*-axis (along the Re chains) and the *a*-axis are labeled. The box shows the unit cell of ReS<sub>2</sub>. (b) Raman spectrum for bulk ReS<sub>2</sub> taken with 515 nm laser excitation ( $\theta = 60^\circ$ ), labeling of the Raman modes, and corresponding eigenvectors for the in-plane ( $A_g^1$ ), out-of-plane ( $A_g^2$ ), and quasi-out-of-plane ( $A_g^3$ ) modes (labeled in red). (c) A schematic of the orientation used in the experiment. The incident and collected polarizations are along the *x*-axis and  $\theta$  is the angle between the *b*-axis and the horizontal. Optical images of (d) 1L and bulk and (e) 2L and 4L of ReS<sub>2</sub> at  $\theta = 0^\circ$ , where the *b*-axis (blue) is aligned along the laser polarization (red). The scale bar is 5  $\mu\text{m}$ .

remains uncertain both experimentally<sup>10,14–17</sup> and theoretically.<sup>10,17–21</sup> Photodetectors fabricated from ReS<sub>2</sub> display high responsivity (88 600 A/W for pristine few-layer ReS<sub>2</sub>, an order of magnitude higher than for monolayer MoS<sub>2</sub>) for applications in weak signal detection.<sup>22,23</sup> Its optical and electronic properties are highly anisotropic in the basal plane, including vibrational modes,<sup>13,24,25</sup> photoluminescence (PL) spectra,<sup>14</sup> and transport properties.<sup>11,21</sup> Lattice-orientation dependent applications in 2D logic circuits,<sup>11</sup> thin film polarizers,<sup>26</sup> strain sensors,<sup>27</sup> and polarization-sensitive photodetectors<sup>28,29</sup> can be realized via ReS<sub>2</sub> that are not possible with the higher-symmetry 2H TMDs. Additionally, ReS<sub>2</sub>, as well as its counterpart ReSe<sub>2</sub>, does not show any obvious degradation when exposed to ambient conditions,<sup>25,30</sup> unlike the other popular anisotropic material, black phosphorus.<sup>31</sup>

Resonant Raman studies of MoS<sub>2</sub> and WS<sub>2</sub> show intriguing results, such as a double resonance of the 2LA(M) mode in monolayer WS<sub>2</sub> at 515 nm that allows for facile identification of monolayer samples.<sup>32–38</sup> Although the angular dependence of the Raman mode intensities for ReS<sub>2</sub> was previously studied by Chenet et al.,<sup>24</sup> a significant question concerning the excitation energy effects on the Raman spectra still remains. In this report, we analyze the Raman spectra of varying thicknesses of ReS<sub>2</sub> using four different excitation wavelengths: 488, 515, 633, and 785 nm, obtaining a Raman response that depends sensitively and intricately on the laser wavelength used to illuminate the sample.

The extra valence electron on the group VII rhenium atoms (compared to tungsten atoms) induces a Peierls distortion of the 1T phase that stabilizes a distorted 1T' phase, forming Re–Re metal bonds along the *b*-axis, as shown in Figure 1a.<sup>11,24</sup> From our density functional theory (DFT) calculations, we find monolayer and bulk ReS<sub>2</sub> to be slightly indirect and indirect gap semiconductors, respectively (Figure S1). Unlike in TMDs with 2H symmetry, which are only centrosymmetric for an even number of layers and bulk, all thicknesses of ReS<sub>2</sub> belong to the  $P\bar{1}$  space group where its unit cell exhibits the symmetry of the  $C_i$  point group (only has inversion symmetry). Thus, all thicknesses of ReS<sub>2</sub> are centrosymmetric. Whereas bulk MoS<sub>2</sub> displays two first-order, higher-frequency ( $>100\text{ cm}^{-1}$ ) modes

in a 180° backscattering configuration (the in-plane  $E_{2g}^1$  and the out-of-plane  $A_{1g}$ ),<sup>39</sup> bulk ReS<sub>2</sub> displays 18 first-order modes within 100–450  $\text{cm}^{-1}$ , as shown in Figure 1b. All of the Raman active modes are of  $A_g$  symmetry, as has been reported previously.<sup>13,40</sup> ReSe<sub>2</sub> exhibits very similar Raman spectra and orientation dependence due to its similar crystal structure to ReS<sub>2</sub>, although its phonon modes occur at lower frequencies (100–300  $\text{cm}^{-1}$ ).<sup>30,41,42</sup> We adopt the indexing scheme of Pradhan et al.<sup>13</sup> for ReS<sub>2</sub> in which the in-plane mode near 150  $\text{cm}^{-1}$  is labeled as  $A_g^1$ , the out-of-plane mode around 437  $\text{cm}^{-1}$  where just the S atoms vibrate is labeled as  $A_g^2$ , and a quasi-out-of-plane mode around 418  $\text{cm}^{-1}$  where the S vibrations are at a slight angle with respect to the basal plane is labeled as  $A_g^3$ . These modes are highlighted in red in Figure 1b along with their eigenvectors. All other modes in which the atoms vibrate at varying angles (due to the low symmetry of ReS<sub>2</sub>) are labeled in order of their increasing frequency from  $A_g^4$  to  $A_g^{18}$ , and their eigenvectors are shown in the Supporting Information (Figure S2).

Another consequence of the Re–Re bonds along the *b*-axis is that exfoliated flakes tend to be cleaved along the two lattice vectors of the crystal in a 60°/120° quadrilateral fashion due to the lower energies of terminating at these edges.<sup>11</sup> This provides a facile way to determine the crystal axes of the flake, although its chirality (i.e., whether the flake is facing “up” or “down”) must also be taken into consideration since there is an absence of mirror symmetry about the midline of the 2D layer in ReS<sub>2</sub>.<sup>43</sup> For this study, ReS<sub>2</sub> was grown by chemical vapor transport (see Methods) and then mechanically exfoliated onto 285 nm SiO<sub>2</sub>/Si(100) substrates. Flakes of one layer (1L), two layers (2L), four layers (4L), and bulk that cleaved in a 60°/120° fashion were chosen (Figure 1d and e). Layer numbers were determined by the frequencies of the layer breathing and shear modes,<sup>25,44</sup> as detailed in Figure S3. The *b*-axis was determined by the polarization-dependent Raman response of  $A_g^7$ , which has a maximum intensity along the *b*-axis for  $\lambda = 532\text{ nm}$  (see Figure S4).<sup>24,43</sup> By comparing optical images, spectra, polar plots (Figure S5), and data from Hart et al.,<sup>43</sup> we are confident that, although mechanical exfoliation produced flakes in both the “up” and “down” orientation on the SiO<sub>2</sub>/Si

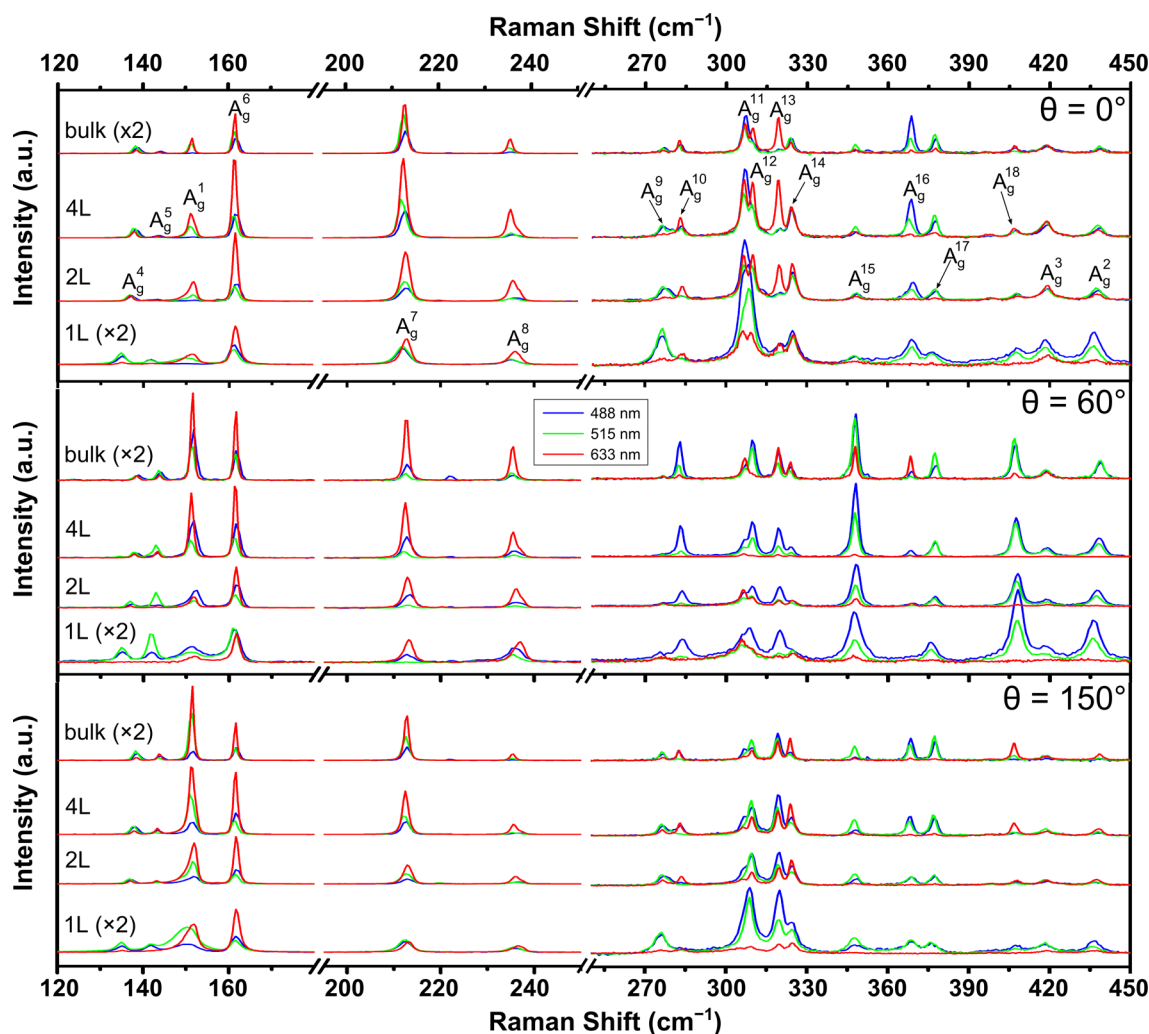


**Figure 2.** Wavelength-dependent Raman for 1L, 2L, 4L, and bulk ReS<sub>2</sub> for  $\theta = 0^\circ$  (top),  $\theta = 60^\circ$  (middle), and  $\theta = 150^\circ$  (bottom). Laser excitations shown are 488, 515, and 633 nm. For ease of comparison, the 1L and bulk spectra were all multiplied by 2. In addition, the frequency range from 250 to 450  $\text{cm}^{-1}$  is on a different vertical scaling and offset than from 120 to 250  $\text{cm}^{-1}$  for clarity. All spectra are normalized to the 520.5  $\text{cm}^{-1}$  Si peak and corrected for the Si angle dependence, resonance behavior, and optical enhancement factors due to multiple reflections in the thin film system. Spectra on the same scaling/offset and including 785 nm are shown in Figures S13 and S14.

substrate, the 1L, 2L, 4L, and bulk flakes studied here are all facing “up” as defined in Figure 1a and c. Furthermore, in comparison with Qiao et al.,<sup>45</sup> we have verified that the 2L, 4L, and bulk flakes all have the same stacking (Figure S6).

The polarized Raman response was analyzed at four different laser excitations: 488 nm (2.54 eV), 515 nm (2.41 eV), 633 nm (1.96 eV), and 785 nm (1.58 eV). Raman spectra were measured in ambient conditions using a 180° backscattering geometry in a parallel polarization configuration in which the incident and scattered polarization were oriented along the horizontal, as shown in the schematic of Figure 1c. The crystal was then rotated by an angle  $\theta$  measured from the direction of the polarization to the  $b$ -axis of the flake. Thus, at  $\theta = 0^\circ$ , the  $b$ -axis was oriented along the horizontal, as shown in Figure 1d and e. Raman spectra were measured for all four laser wavelengths at three distinct angles:  $\theta = 0^\circ$  (laser polarization along  $b$ -axis),  $\theta = 60^\circ$  (laser polarization along  $a$ -axis), and  $\theta = 150^\circ$  (laser polarization perpendicular to the  $a$ -axis where the in-plane mode  $A_g^1$  is near a maximum intensity at  $\lambda = 515$  nm, see Figure S4).

All of the Raman spectra and phonon intensities shown in this manuscript have been normalized to a reference Si phonon mode at 520.5  $\text{cm}^{-1}$  (measured off of the ReS<sub>2</sub> sample but close by) and then corrected for the polarization-dependent intensity of the Si(100) mode,<sup>46</sup> resonant behaviors of Si,<sup>47</sup> and the optical enhancement due to multiple reflections at the boundaries between the interfaces,<sup>48–50</sup> including ReS<sub>2</sub>–SiO<sub>2</sub> and SiO<sub>2</sub>–Si, as is extensively detailed in the Supporting Information (pages S8–S16). For thin TMDs on SiO<sub>2</sub>/Si substrates, multiple reflections in the SiO<sub>2</sub> layer (negligible absorption in the measured spectral range) are primarily responsible for the optical enhancement effect. Since the enhancement depends strongly on both the complex index of refraction and the wavelength of light used, it is important to consider when interpreting our resonant Raman experiments. Moreover, we must also account for a normalization factor in the optical enhancement calculations that considers the air–ReS<sub>2</sub>–air and air–Si–air boundaries that, while included in earlier graphene studies<sup>45</sup> and one reference on MoS<sub>2</sub>,<sup>49</sup> has been absent in other recent reports on TMDs. Although the lack of normalization factors did not appear to have a significant

impact on the overall enhancement factor for other TMDs,<sup>32,50,51</sup> for ReS<sub>2</sub> the non-normalized enhancement factor was unrealistically large due to the values of the real and complex parts of the index of refraction (see [Supporting Information](#)). For example, the non-normalized enhancement factor ratio between the 785 nm and 488 nm cases is around 215:1 for monolayer ReS<sub>2</sub>, respectively, while the same ratio is 15:1 with correct normalization. Proper correction for the optical interference effect is thus vital to capturing intrinsic resonance properties of 2D materials.

Raman spectra after the correction procedures for the four different number of layers (1L, 2L, 4L, and bulk), three polarization angles ( $\theta = 0^\circ$ ,  $60^\circ$ , and  $150^\circ$ ), and three of the laser excitations (488, 515, and 633 nm) are shown in [Figure 2](#). Spectra including 785 nm laser excitation are shown in [Figure S14](#) in the [Supporting Information](#). [Figure 2](#) reveals that the intensity ratios  $[I(A_g^x)/I(A_g^y)]$ , where  $I$  is the intensity of the mode] of the Raman modes depends sensitively on the laser excitation wavelength, the number of ReS<sub>2</sub> layers, and the polarization angle  $\theta$ . More importantly, individual intensity ratios change *differently* as a function of laser excitation, layer count, and polarization angle; no single mode demonstrates a consistent intensity throughout the parameter space and each mode behaves uniquely. As there are too many individual intensity ratios to discuss here, we focus on one quantitative example,  $I(A_g^1)/I(A_g^6)$ , to demonstrate the impact of the  $\lambda$ , layer number, and  $\theta$ . [Table 1](#) gives this intensity ratio for 488, 515,

**Table 1. Intensity Ratios  $I(A_g^1)/I(A_g^6)$  for Three Laser Excitation Wavelengths and Three Polarization Angles**

$\lambda$ (nm)	energy (eV)	$I(A_g^1)/I(A_g^6)$			
		1L	2L	4L	bulk
$\theta = 0^\circ$					
488	2.54	0.03	0.04	0.03	0.03
515	2.41	0.19	0.40	0.46	0.53
633	1.96	0.19	0.25	0.28	0.37
$\theta = 60^\circ$					
488	2.54	0.40	0.66	1.06	1.53
515	2.41	0.15	0.47	0.77	1.57
633	1.96	0.22	0.22	0.80	1.21
$\theta = 150^\circ$					
488	2.54	0.30	0.40	0.56	0.67
515	2.41	1.22	2.20	2.70	4.89
633	1.96	0.46	0.72	1.06	1.93

and 633 nm laser wavelengths. [Figure 2](#) and [Table 1](#) show that, when the laser polarization is along the  $b$ -axis ( $\theta = 0^\circ$ ),  $I(A_g^1)/I(A_g^6)$  is less than 1 for all thicknesses and wavelengths. In contrast, when the laser polarization along the  $a$ -axis ( $\theta = 60^\circ$ ),  $I(A_g^1)/I(A_g^6)$  is *thickness* dependent, increasing as the thickness increases for all three of the wavelengths. Furthermore, when the laser polarization is perpendicular to the  $a$ -axis ( $\theta = 150^\circ$ ),  $I(A_g^1)/I(A_g^6)$  is both *thickness* and *wavelength* dependent. When excited with 488 nm at  $\theta = 150^\circ$ ,  $A_g^1$  is always weaker than  $A_g^6$ , while at 515 nm laser excitation,  $A_g^1$  is always stronger than  $A_g^6$ , both of which are independent of the number of layers. For 633 nm laser excitation, on the other hand,  $A_g^1$  starts out weaker than  $A_g^6$  for 1L and 2L, but becomes more intense than  $A_g^6$  for 4L and bulk. Thus, the intensity ratios of the modes as a function of laser wavelength depend sensitively and intricately on both the thickness and the orientation of the ReS<sub>2</sub> crystal. Moreover, the discussion above covers only one example ratio:

[Table S1](#) details that the ratio  $I(A_g^7)/I(A_g^8)$ , for example, has a completely different behavior as a function of  $\lambda$ , number of layers, and  $\theta$ .

How specific modes behave (relative to the other modes) is also unique for the different laser excitation energies, the number of layers, and sample orientation. For example, certain modes are only present at specific wavelengths, such as the in-plane mode  $A_g^1$  at  $\theta = 0^\circ$ , which shows a large intensity for 515 and 633 nm laser excitations but is barely present for 488 nm. At  $\theta = 60^\circ$ ,  $A_g^2$ ,  $A_g^3$ ,  $A_g^4$ ,  $A_g^5$ , and  $A_g^{18}$  are all absent for 1L at 633 nm but are strong at 488 and 515 nm. This previous example at  $\theta = 60^\circ$  is also thickness-dependent, in that the modes increase in intensity as the layer number increases up to bulk. In general, when comparing  $\lambda = 488$ , 515, and 633 nm, the intensities of  $A_g^1$ ,  $A_g^6$ ,  $A_g^7$ , and  $A_g^8$ , which are predominantly Re in-plane vibrations, are stronger at 633 nm, especially for 4L and bulk, while the modes with a predominantly S vibration ( $250\text{ cm}^{-1}$  to  $450\text{ cm}^{-1}$ ) are stronger at 488 and 515 nm than at 633 nm. When considering 785 nm ([Figure S14](#)), the intensities of the predominantly S vibrations, especially  $A_g^8$  and  $A_g^{12}$ , dominate the spectra at all three angles. It should be noted that we do not observe an overall increase in the intensity of all of the modes at any laser wavelength. Instead, we see increases in the intensity of some modes relative to others. Even at  $\lambda = 785\text{ nm}$ , where the intensities of the predominantly S vibrations are large, the intensities of the other modes (i.e., below  $250\text{ cm}^{-1}$ ) are similar to the intensities at 488, 515, and 633 nm.

Changes in the behavior of the modes can also be seen by studying the percentage change in intensity for each mode, with respect to the mode's intensity at 488 nm laser excitation:  $\Delta I(\lambda) = \frac{I(\lambda) - I(488)}{I(488)} \times 100\%$ . [Figure 3](#) shows  $\Delta I(\lambda)$  for the first six modes as well as some of the higher frequency modes as a function of the laser excitation energy and number of layers for  $\theta = 0^\circ$ , when the laser polarization is along the  $b$ -axis. The modes are separated into  $A_g^1$ ,  $A_g^6$ ,  $A_g^7$ ,  $A_g^8$  ([Figure 3a](#), predominantly Re in-plane vibrations),  $A_g^4$ ,  $A_g^5$  ([Figure 3b](#), predominantly Re out-of-plane vibrations), and  $A_g^{12}$ ,  $A_g^{15}$ ,  $A_g^{16}$ ,  $A_g^{18}$ ,  $A_g^3$ ,  $A_g^2$  ([Figure 3c](#), predominantly S vibrations), based on their eigenvectors. Two-dimensional versions of these graphs for each layer thickness are shown in [Supplementary Figures S16 and S17](#). Interestingly, grouping the modes this way allows general trends in the percentage change in intensity at specific wavelengths to be discerned. For  $A_g^6$  and  $A_g^7$ , which are predominantly Re in-plane vibrations, the maximum percentage change in intensity occurs at 1.96 eV, although the values are relatively small (<250%). On the other hand, for  $A_g^1$  and  $A_g^8$ , the percentage change in intensity is much larger (as high as 4500%) due to the small intensity of these phonon modes at 2.54 eV. The fully in-plane mode,  $A_g^1$ , peaks at 1.96 eV for 2L and 4L but peaks at 1.58 eV for 1L and bulk.  $A_g^8$  however, is always maximized at 1.58 eV. For the predominantly Re out-of-plane vibrations  $A_g^4$  and  $A_g^5$  ([Figure 3b](#)), the maximum percentage change in intensity at 1.58 eV is less than 1250% while the S dominated vibrations in [Figure 3c](#) (higher frequency modes  $A_g^{12}$ ,  $A_g^{15}$ ,  $A_g^{16}$ ,  $A_g^{18}$ ,  $A_g^3$ ,  $A_g^2$ ) have extremely large intensity changes (up to  $\sim 13\,000\%$  for  $A_g^{12}$ ) maximized at 1.58 eV. However, the behavior and magnitude of the percentage change in intensity as a function of wavelength for the modes described above are highly anisotropic, as shown in [Figure S18](#) where  $\theta = 0^\circ$ ,  $60^\circ$ , and  $150^\circ$  are compared. For example,  $A_g^7$  has a maximum percentage change in intensity of  $\sim 250\%$  at 1.96 eV for both  $\theta = 0^\circ$  and  $\theta = 150^\circ$ , whereas at  $\theta =$

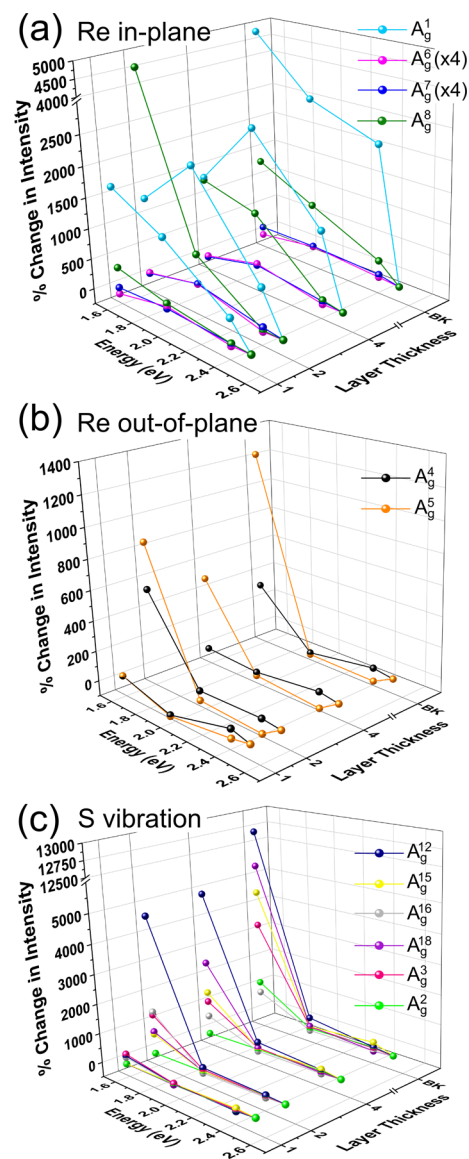


**Figure 3.** Change in intensities ((%), with respect to the Si normalized intensity at 488 nm) for (a)  $A_g^1$ ,  $A_g^6$ ,  $A_g^7$ ,  $A_g^8$ , (b)  $A_g^4$ ,  $A_g^5$ , and (c)  $A_g^{12}$ ,  $A_g^{15}$ ,  $A_g^{16}$ ,  $A_g^{18}$ ,  $A_g^3$ , and  $A_g^2$  as a function of laser energy and layer thickness,  $\theta = 0^\circ$ . The modes are predominantly (a) Re in-plane, (b) Re out-of-plane, and (c) S vibrations. The % change in intensity was multiplied by 4 for  $A_g^6$  and  $A_g^7$  for the ease of comparison. Lines are drawn to guide the eyes.

$60^\circ$  the maximum percentage change in intensity is significantly higher (up to  $\sim 2000\%$ ) and located at 1.58 eV. This agrees with theoretical reports predicting the extremely anisotropic absorption properties in  $\text{ReS}_2$ .<sup>20</sup>

To understand our results, we consider resonant Raman studies on  $\text{MoS}_2$  and  $\text{MoSe}_2$ , which observed that the first-order Raman mode intensities are significantly increased at excitonic transitions due to dominating electron–photon interactions.<sup>32,51</sup> Recently, reflection contrast measurements confirmed that mono- and few-layer  $\text{ReS}_2$  display three main excitons in the range from 1.3 to 2.1 eV.<sup>14</sup> For monolayer  $\text{ReS}_2$ , exciton 1, exciton 2, and exciton 3 are located at approximately 1.6, 1.68, and 1.88 eV, respectively, in which the energies of the excitons all decrease as the thickness is increased, as shown in Figure S20. The 1.58 eV laser excitation is below the lowest

exciton transition for the monolayer, which we postulate is the reason for the extremely low signal observed for the 1L flake using the same collection parameters (power, integration time, etc.) as the 2L, 4L, and bulk samples. A laser excitation of 1.96 eV, on the other hand, is close to exciton 3 (1.88 eV) in the monolayer, which would explain the maximum percentage intensity change at 1.96 eV nm for  $A_g^6$  and  $A_g^7$ . However, the energy of exciton 3 rapidly decreases with additional layers, already reaching 1.72 eV for the bilayer. Thus, this exciton cannot explain the maximum percentage change in intensity at 1.96 eV for the other layer thicknesses. For few-layer  $\text{ReS}_2$ , the 1.58 eV laser excitation is close to the levels of both excitons 1 and 2. Thus, our data supports that the maximum intensity of many of the modes at 1.58 eV corresponds to an increased absorption at this exciton resonance condition. As the laser energy increases beyond the  $\text{ReS}_2$  band gap, we find that the Raman intensities of certain modes reach peak values at 1.96 eV when the absorption (electron–photon) interactions are not peaked (i.e., not at excitonic transitions). As this is not an overall increase of all of the modes, it indicates that the electron–phonon interaction, whose strength also determines Raman intensities (see Methods), is strong between these phonon modes and the electronic states on resonance.

Unlike the dependence of the first-order Raman intensities on laser energy in  $\text{MoS}_2$  (also known as the Raman excitation profile),<sup>32</sup> which simply resembles the features of its absorption spectra, the complex dependence of Raman intensities on layer number, polarization angle, and laser energy in  $\text{ReS}_2$  provides a challenging opportunity to test the computation of Raman intensities from first principles. Gillet et al.<sup>52</sup> recently proposed calculating resonant Raman intensities based on finite differences where the frequency-dependent dielectric function is calculated twice for each Raman-active phonon mode by solving the Bethe–Salpeter equation. However, the computation time required for the finite-difference approach scales with the total number of degrees of freedom and is therefore impractical for  $\text{ReS}_2$  with 18 Raman-active phonon modes. We therefore implemented a perturbation approach for calculating resonant Raman intensities from first-principles in which frequency-dependent optical transition matrix elements are only calculated once, at the small additional cost of calculating the electron–phonon coupling matrix elements for each mode (see Methods for details).

The calculations performed herein do not yet include quasiparticle or excitonic effects due to the demanding computational requirement for monolayer  $\text{ReS}_2$ , which contains 12 atoms per unit cell and requires sampling half of the Brillouin zone due to its low symmetry (inversion symmetry cannot be exploited). Therefore, the current level of theory does not aim to quantitatively describe the prolific Raman-active phonons of  $\text{ReS}_2$  and their respective dependences on excitation energy, polarization angle, and layer number. We instead identify and focus on the following two main classes of features, assuming that quasiparticle or excitonic effects would not substantially alter the results: (1) All 18 first-order Raman intensities on-resonance with the lowest direct gap for 1L and bulk are calculated and compared with the measured intensities for the 785 nm laser and (2) laser wavelength dependence is examined by comparing the calculated Raman intensities at 785 nm ( $\sim 1.6$  eV) and 633 nm ( $\sim 2$  eV), showing that the Raman modes above  $250 \text{ cm}^{-1}$ , i.e., the predominantly S vibrations, are significantly more intense at the 785 nm resonance. The DFT bandgap (1.42 eV for monolayer) and the excitation energies

were shifted up in all calculations such that the calculated monolayer bandgap matches the experimentally reported value of 1.61 eV for monolayer.<sup>14</sup> We further note that, experimentally, the 785 nm laser wavelength (1.58 eV) is actually closer to the lowest exciton level of a bilayer (1.56 eV) and below that of a monolayer (1.61 eV), yielding a very small signal-to-noise ratio for monolayer (due to being off-resonance), making a comparison intractable. To overcome this, we compared the calculated results for the *monolayer* with the measured spectra of the *bilayer*. For clarity, the polarization of the incident and collected light for all of the calculations are chosen to be at  $\theta = 120^\circ$ , where the absorption for 1L ReS<sub>2</sub> is maximized.<sup>20</sup>

As shown in Figure 4a, the on-resonance (at lowest direct-gap) Raman spectra for 1L ReS<sub>2</sub> (red) calculated from first-

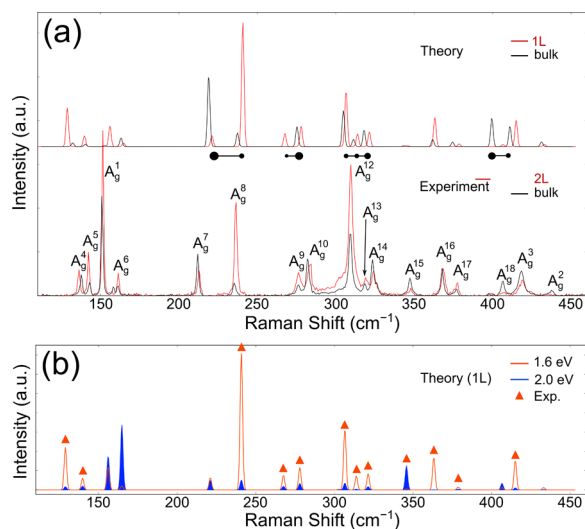


**Figure 4.** (a) Raman spectra calculated using DFT (upper panel) for 1L (red) and bulk (black) ReS<sub>2</sub> for excitation energies on resonance with the lowest optical transition (i.e., across the smallest direct gap of 1.6 eV). The connected black dots schematically show the calculated change in relative intensity among each group of modes when going from monolayer (red) to bulk (black); i.e., a larger dot in a connected group indicates the relative intensity of that Raman mode (compared with other peaks in the group) increased when going from monolayer to bulk, and vice versa. These intensity trends are compared with experimentally measured Raman spectra (lower panel) for 2L (red) and bulk (black) at 1.58 eV (785 nm) laser excitation and  $\theta = 150^\circ$  (see main text for details). (b) Comparing the DFT-calculated Raman intensities for monolayer ReS<sub>2</sub> at two different excitation energies, 1.6 eV (orange) and 2.0 eV (blue). Modes that were experimentally shown to dominate at 1.58 eV laser energy, where the measured intensities are more than doubled going from 1.96 eV (633 nm) to 1.58 eV, are highlighted with orange triangles. For all Raman intensity calculations, the five lowest conduction bands and five highest valence bands were taken into account.

principles (top panel) captures the experimentally measured intensities ( $\lambda = 785$  nm, 2L, bottom panel) for all modes above 200 cm<sup>-1</sup>, including the strong intensities of the A<sub>g</sub><sup>8</sup> and A<sub>g</sub><sup>12</sup> modes observed at all three angles measured (see Figure S14). Raman intensities for bulk (black) show a similar level of agreement between theory and experiment. The discrepancies for the modes lower than 200 cm<sup>-1</sup> are likely due to their strong dependence on polarization (see Figure S14), a question reserved for future work. The connected groups of black dots in Figure 4a highlight the changes in relative intensities among

each group of modes when the thickness increases from 1L to bulk, which can provide useful additional signatures to characterize the number of layers. For example, A<sub>g</sub><sup>7</sup> becomes larger than A<sub>g</sub><sup>8</sup> when going from 1L to bulk, as is shown schematically in the larger size of the dot under A<sub>g</sub><sup>7</sup>.

In Figure 4b, the calculated Raman intensities for 1L ReS<sub>2</sub> for two excitation energies, 1.6 eV (orange and unfilled) and 2.0 eV (blue and filled), are compared. Modes that were experimentally shown to dominate at 1.58 eV laser excitation (i.e., the modes for which the experimentally measured intensities are more than doubled when going from 1.96 to 1.58 eV) are highlighted with orange triangles. For the modes characterized by predominantly S vibrations (250 cm<sup>-1</sup> to 450 cm<sup>-1</sup>), an overall increase in intensity is seen in the calculated results and is consistent with experiments (orange triangles) in 8 out of 9 cases, the exception being the A<sub>g</sub><sup>15</sup> mode. For the modes involving primarily Re vibrations (120 cm<sup>-1</sup> to 250 cm<sup>-1</sup>), all three of the experimentally dominant modes at 1.58 eV excitation energy (A<sub>g</sub><sup>4</sup>, A<sub>g</sub><sup>5</sup>, and A<sub>g</sub><sup>8</sup>) are accurately reproduced by theory. Additional calculations including excitonic effects are expected to increase the predicted Raman intensities when the excitation energy closely matches the excitonic levels (due to the discreteness of excitonic levels), for example, at 1.58 eV (785 nm). The calculations presented herein, despite the lack of excitonic effects, encourage additional resonant Raman experiments with tunable laser sources to study further the complex layer-, polarization angle-, and mode-dependent Raman resonance profiles in ReS<sub>2</sub>.

Remarkably, we observed additional peaks beyond the assigned 18 first-order modes that have not been discussed in previous reports,<sup>10,11,24,25,40,44</sup> as shown in Figure 5. Many of these additional peaks have intensities with a clear thickness dependence, such as the shoulder peak “ $\omega_1$ ” at a lower frequency than the in-plane mode A<sub>g</sub><sup>1</sup> (Figure 5a) and the shoulder “ $\omega_2$ ” at higher frequency than A<sub>g</sub><sup>8</sup> (Figure 5b), both of which decrease in intensity as the thickness increases. Illuminating ReS<sub>2</sub> with  $\lambda = 785$  nm exposed numerous new peaks between 125 and 300 cm<sup>-1</sup>, as shown in Figures 5c, S14, and S15. The 4L flake showed the largest number of additional peaks, as detailed in Figure 5c, where those marked with an orange asterisk are in addition to the already-assigned 18 first-order modes. The peak between A<sub>g</sub><sup>1</sup> and A<sub>g</sub><sup>6</sup> (around 157 cm<sup>-1</sup>) is present in other thicknesses, increasing in intensity from 2L up to bulk (see Figure S15). The other peaks, however, are only observed in the 4L flake. Within the spectral resolution of the spectrometer and the uncertainty in Lorentzian fitting, the frequencies of the extra peaks are consistent (within 1 cm<sup>-1</sup>) at the different laser wavelengths. Some of these modes have been observed previously, although they are not discussed by the authors.<sup>44</sup>

To shed light on possible origins of these peaks, we calculated the phonon dispersion along  $\Gamma$ -M-K- $\Gamma$  and the phonon density of states (PhDOS) for monolayer ReS<sub>2</sub>, as shown in Figure 5d up to 320 cm<sup>-1</sup>. The first-order Raman-active modes at  $\Gamma$  are labeled in red with horizontal lines connecting the phonon dispersion to the PhDOS. In addition to the Raman-active modes, there are also infrared-active modes at the  $\Gamma$  point with A<sub>u</sub> symmetry, many of which are close in frequency to the Raman-active modes. It is possible that disorder-induced activation of the infrared-active modes in the ReS<sub>2</sub> occurs due to the breaking of inversion symmetry, thus lifting the complementarity of Raman and IR activity. No IR-active branch exists within 10 cm<sup>-1</sup> below (above) A<sub>g</sub><sup>1</sup> (A<sub>g</sub><sup>8</sup>)

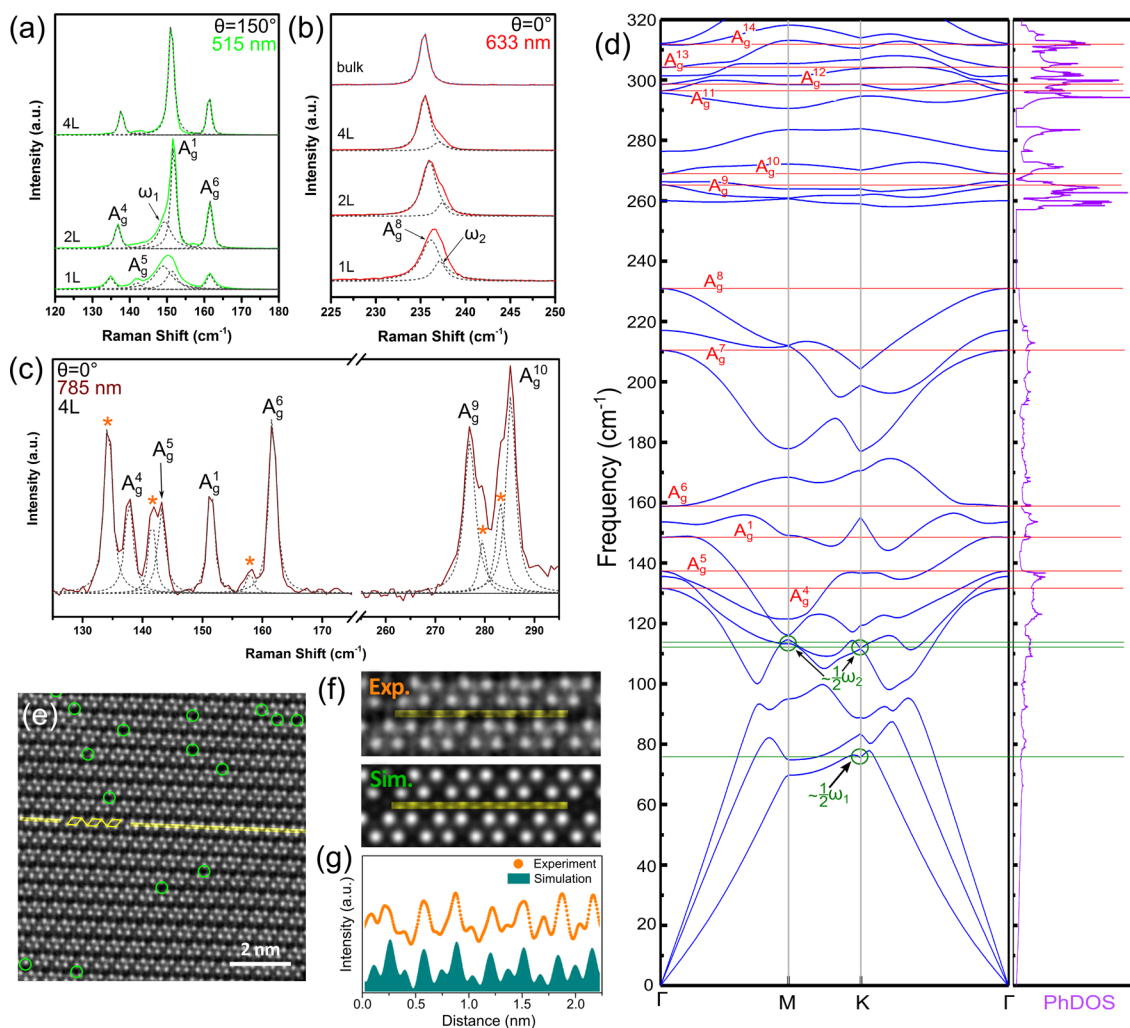


**Figure 5.** (a) Shoulder  $\omega_1$  is observed at a lower energy than first-order mode  $A_g^1$  ( $\sim 150$   $\text{cm}^{-1}$ ), whereas (b) shoulder  $\omega_2$  is observed at higher energy than the first order mode  $A_g^8$  ( $\sim 235$   $\text{cm}^{-1}$ ). (c) New peaks (highlighted with \*) are observed in the 4L sample at  $\lambda = 785$  nm. (d) Phonon dispersion and density of states (PhDOS, right) for monolayer  $\text{ReS}_2$  up to  $320$   $\text{cm}^{-1}$ . The first-order Raman-active modes at  $\Gamma$  are labeled and marked by red lines. (e) High-resolution scanning transmission electron microscopy (HRSTEM) of monolayer  $\text{ReS}_2$ . Green circles indicate defects in the lattice, mostly consisting of S vacancies, identified by comparing experimental and simulated STEM annular dark field (STEM-ADF) images, as shown in panel f. The line profile in panel g was acquired along the yellow line in panel f.

where  $\omega_1$  ( $\omega_2$ ) is observed, yet there is an IR-active branch between  $A_g^1$  and  $A_g^6$  that could account for the peak observed at  $157$   $\text{cm}^{-1}$  (Figure 5c). Another possibility is defect-mediated non- $\Gamma$  point modes, yet no Raman-active branch exists at the higher symmetry M or K points near the frequency of  $\omega_1$  ( $\omega_2$ ), which is observed at a lower (higher) frequency than  $A_g^1$  ( $A_g^8$ ). At the K point, there are bands that correspond to approximately half the frequency of  $\omega_1$  and  $\omega_2$  with small peaks in the PhDOS. For  $1/2 \omega_2$ , there is also a band at the M point with a peak in the PhDOS. This suggests that  $\omega_1$  and  $\omega_2$  could be attributed to double resonance processes involving M- or K-point phonons.<sup>51</sup> The small change of the bandgap in  $\text{ReS}_2$  with increasing layer number could explain that, if  $\omega_1$  and  $\omega_2$  are double resonance processes, their intensity would be influenced by the thickness of the flake since double resonance processes are very sensitive to the electronic structure.<sup>10,11,53</sup> New first-order modes only present in few-layer 2H-TMDs (e.g.,  $\text{WSe}_2$ ,  $\text{MoS}_2$ ,  $\text{WS}_2$ ) have also been theoretically and experimentally discovered by Terrones et al., including out-of-plane modes with both the metal and chalcogen atoms vibrating and Raman-active splitting modes.<sup>54</sup> For example,

the calculated phonon dispersion of  $\text{WSe}_2$  shows that, while mono- and bilayers display one perpendicular mode, tri-, tetra-, and pentalayers have two, two, and three branches, respectively. If similar trends in the number of phonon branches for varying layer thicknesses also occur for 1T'  $\text{ReS}_2$ , then additional branches in the phonon dispersion could explain why the 4L  $\text{ReS}_2$  flake displayed more modes than the 1L or 2L flakes.

To investigate the quality of our material, exfoliated flakes of  $\text{ReS}_2$  from the same crystal batch were transferred onto a SiN/Si grid for high-resolution scanning transmission electron microscopy (HRSTEM) (see Methods). Figure 5e shows the HRSTEM of monolayer  $\text{ReS}_2$ , where the direction of the  $b$ -axis along the Re–Re chains is highlighted in yellow. By comparing experimental and simulated STEM annular dark field (STEM-ADF) images and line scans, as shown in Figure 5f and g, respectively, point defects were identified in the lattice. These defects, mostly consisting of sulfur vacancies, are highlighted by green circles in Figure 5e, although it remains unclear if some of these vacancies were created by the electron beam irradiation. Possible effects of these sulfur vacancies on the Raman spectra

of ReS<sub>2</sub> and whether they can be playing a role in the appearances of new modes is reserved for future work.

In conclusion, Raman spectroscopy, which is used extensively and broadly within the 2D research community, is an extremely powerful tool to investigate the photophysics of anisotropic materials. By correctly accounting for thin film interference effects, which is imperative for 2D materials on SiO<sub>2</sub>/Si substrates, we revealed the resonant Raman behavior for varying number of layers of ReS<sub>2</sub> using four excitation wavelengths. Our results demonstrate that the already rich Raman spectrum of ReS<sub>2</sub> is further complicated by the differing behavior of these modes as a function of laser excitation wavelength. Moreover, the laser-dependent Raman response is also affected by number of layers as well as the orientation of the crystal with respect to the laser polarization. Each of the 18 first-order phonons has its own unique behavior as a function of laser excitation, thickness, and orientation. Thus, it is imperative to take all parameters into account when using Raman spectroscopy to discern the physical properties of ReS<sub>2</sub> as well as other anisotropic 2D materials. Our experimental results indicate that the resonant Raman behavior of the modes can be grouped by vibrational eigenvectors (i.e., predominantly Re in-plane, Re out-of-plane, and S vibrations) and that many of the modes, especially the S vibrations, are enhanced near the energy of the lowest exciton (~1.6 eV). Unlike in 2H materials such as MoS<sub>2</sub> and MoSe<sub>2</sub>, we observe that certain modes in ReS<sub>2</sub> are more enhanced at laser energies not corresponding to absorption peaks (as opposed to an overall increase in intensity of *all* of the first-order modes at laser energies that align with peaks in the absorption), which suggests that the contributions of electron–phonon coupling for these specific modes dominate over those of the electric–photon interaction. By adapting a perturbation approach at the DFT level, we calculated the resonant Raman intensities of this low-symmetry material and theoretically confirmed many of the observed wavelength dependent behaviors. This perturbation approach scales favorably with respect to the number of Raman modes (compared with existing methods using finite differences), especially for anisotropic materials with lower symmetry. Calculations considering excitonic effects and orientation are still necessary to fully understand the resonant Raman behavior in ReS<sub>2</sub>. Potential origins of the additional modes observed in our samples were discussed using the phonon dispersion of monolayer ReS<sub>2</sub>, including defect-activated IR modes, defect-mediated non- $\Gamma$  point modes, and double resonance processes. This study indicates that the interplay between incident laser energy, orientation, and layer thickness on the numerous phonon modes of ReS<sub>2</sub> is indeed more intricate, and thus more intriguing, than for its 2H counterparts.

**Methods.** *ReS<sub>2</sub> Crystal Growth.* ReS<sub>2</sub> bulk crystals were synthesized by sealing Re powder (99.99%) and S pieces (99.9995%) in a stoichiometric ratio in a quartz ampule under vacuum with 2.7 mg/cm<sup>3</sup> of iodine (99.999%). Subsequently, the material was heated to 1080 °C over a period of 24 h with a 100 °C temperature difference between the hot and cold zones of the ampule and held at that temperature for 1 week. Afterward, the sample was cooled to room temperature at a rate of 100 °C/h. The samples were then removed and rinsed in acetone and isopropyl alcohol to remove any excess iodine on the surface of the single crystals. Mechanical exfoliation using adhesive tape was performed, and the micron-sized flakes were transferred onto a Si(100) substrate with a SiO<sub>2</sub> thickness of 285 nm grown by thermal oxidation.<sup>55</sup>

*Raman Measurements.* Raman spectra for 487.987, 514.5308, and 632.817 nm laser excitations were measured at room temperature using a triple-grating Raman spectrometer (Horiba JY T64000 with a 100 $\times$ , objective, N.A. 0.9) coupled to a CCD detector that was cooled with liquid nitrogen. For the 785 nm laser excitation, spectra were recorded using a single-grating spectrometer (Renishaw inVia micro-Raman, 1800 lines/mm grating, 50 $\times$  objective, N.A. 0.75) due to wavelength limitations of the microscope attached to the triple-grating spectrometer. All spectra were taken in the 180° backscattering configuration. For the triple-grating spectrometer, the lasers are linearly polarized in the horizontal direction with respect to the stage, and a linear polarizer and half-wave plate were used as analyzers to collect scattered light in the parallel polarization configuration. Polarization orientations were confirmed using a MoS<sub>2</sub> reference sample.<sup>56</sup> For the single-grating spectrometer, the 785 nm laser excitation is linearly polarized, and a linear polarizer was used as an analyzer to collect parallel scattered polarization. Integration times ranged between 10 and 13 min, and the power was kept at approximately 200  $\mu$ W through the objective. The spectra were normalized to the intensity of the silicon peak at 520.5 cm<sup>-1</sup> measured near the ReS<sub>2</sub> flake, and the intensity was corrected for the angle dependence of silicon (100),<sup>41</sup> resonant behavior of the silicon,<sup>47</sup> and optical enhancement due to thin film interference effects,<sup>48–50</sup> as detailed in the [Supporting Information](#).

*First-Principles Calculations.* Resonant Raman intensities were calculated following a perturbation approach at the single-particle level (considering only Stokes lines)<sup>57</sup>

$$\chi_i(\omega_L) \sim \sum_{c,v,k} \frac{\langle vk|H_{e-R}|ck\rangle(\langle ck|H_{e-ph}|ck\rangle - \langle vk|H_{e-ph}|vk\rangle)\langle ck|H_{e-R}|vk\rangle}{(\omega_L - \omega_{ck} - i\gamma)(\omega_L - \omega_{ck} - \omega_\lambda - i\gamma)}$$

where  $\omega_L$  is the incident laser energy,  $|ck\rangle$  and  $|vk\rangle$  are conduction and valence band states with momentum  $\mathbf{k}$ ,  $\omega_{ck}$  is their energy difference,  $\omega_\lambda$  is the energy of a phonon branch with index  $\lambda$ , and  $\gamma$  is a damping constant due to the finite lifetime of the intermediate state, taken to be 0.04 eV here. The electron–photon coupling (or, as more commonly used in Raman literature, electron–radiation coupling) is given by

$$\langle v|H_{e-R}|c\rangle = \mathbf{P} \cdot \langle v|\mathbf{r}|c\rangle = -i \lim_{q \rightarrow 0} \frac{\langle v\mathbf{k} + \mathbf{q}_\alpha|e^{i\mathbf{q}\cdot\mathbf{r}}|c\mathbf{k}\rangle}{q}$$

where  $\mathbf{q}_\alpha$  is a small wavevector shift in the direction of  $\mathbf{P}$ , and  $q = |\mathbf{q}_\alpha|$ . The electron–phonon coupling matrix elements are given by

$$\langle i\mathbf{k}|H_{e-ph}|j\mathbf{k}\rangle \sim \sqrt{\frac{1}{2N\omega_\lambda}} \sum_{s,\alpha} \langle i\mathbf{k}|\frac{\partial V_{\text{SCF}}}{\partial R_{s\alpha}}u_{s\alpha}^\lambda|j\mathbf{k}\rangle$$

where  $S$  and  $\alpha$  are indices for the sublattices and Cartesian coordinates,  $u^\lambda$  is the eigenvector for mode  $\lambda$ , and  $V_{\text{SCF}}$  is the Kohn–Sham potential. Both types of matrix elements were sampled on a 12  $\times$  12  $\times$  1  $\Gamma$ -centered grid and interpolated onto a 24  $\times$  24  $\times$  1 grid for monolayer ReS<sub>2</sub> and on an 8  $\times$  8  $\times$  8 grid and interpolated onto a 16  $\times$  16  $\times$  16 grid for bulk ReS<sub>2</sub>.

Electron–phonon coupling calculations (and prerequisite structural relaxations) were performed using the Quantum Espresso (QE) package.<sup>58</sup> The relaxation for bulk ReS<sub>2</sub> requires finite interlayer adhesion, which is only available if one exploits the fortuitous interlayer overbinding using the local density approximation (LDA) exchange–correlation functional or if van

der Waals forces are calculated and superimposed onto the forces calculated within the generalized gradient approximation (GGA); a common combination is the Perdew–Burke–Ernzerhof parametrization (GGA-PBE) and the empirical DFT-D2 method.<sup>59,60</sup> Since the linear response routines in QE does not currently support vdW forces, we resorted to using LDA for both 1L and bulk ReS<sub>2</sub>. As a justification, Raman intensities for 1L ReS<sub>2</sub> were also performed using PBE: the resulting Raman intensities agreed well with the intensities calculated with LDA (only the Raman frequencies changed, by no more than 20 cm<sup>-1</sup>). Electron–ion interactions are described within the projector augmented wave (PAW) formalism.

All band structure and electron–photon coupling matrix elements (and prerequisite structural relaxations) were performed by the Vienna Ab-initio Simulation Package (VASP) also using LDA functionals,<sup>61,62</sup> with energies converged at a plane wave expansion energy cutoff of 400 eV and forces converged at 0.004 eV/Å. Interatomic force constants were calculated using the finite displacement method with a 2 × 2 × 1 supercell (48 atoms). All conduction bands calculated from DFT have been rigidly shifted by 0.2 eV to match with the experimentally measured optical gaps for 1L ReS<sub>2</sub>.<sup>14</sup> For all Raman intensity calculations, the five highest valence bands and five lowest conduction bands were used in the summation, spanning at least 3.0 eV.

**STEM Analysis.** Mechanically exfoliated ReS<sub>2</sub> sheets were transferred from SiO<sub>2</sub>/Si substrates to a SiN/Si TEM grid utilizing a wet etch of the SiO<sub>2</sub>, similar to what was reported previously by Elias et al.<sup>63</sup> The substrates were spin-coated with PMMA (MW 495000, A6) at 2000 rpm for 60 s and cured at 40 °C for at least 4 h. Afterward, the samples were placed in a buffered oxide etch (6:1) for a few hours to etch the SiO<sub>2</sub> until the PMMA/ReS<sub>2</sub> was released from the substrate. The PMMA/ReS<sub>2</sub> was cleaned in three DI water baths before being transferred onto the TEM grid. Once dried, acetone was used to remove the PMMA, leaving ReS<sub>2</sub> flakes on the grid. Scanning transmission electron microscopy (STEM) was carried out by FEI Titan<sup>3</sup> 60–300 G2 S/TEM operated at 80 keV to investigate the atomic structure of the ReS<sub>2</sub> sheet. To reduce irradiation damage, the beam current was kept below 40 pA. A high angle annular dark field (HAADF) detector was used for STEM-ADF imaging. A low-angle annular dark field (LAADF) condition was used rather than a HAADF condition to enhance the contrast from S atoms for the investigation of defects. For the image in the Figure 5, the Gaussian blur filter was applied by *ImageJ* program to reduce the noise and enhance the visibility of detailed structure, but raw images were used for acquiring line profile of the ADF intensity. The STEM-ADF image simulation was conducted using the *QSTEM* package.<sup>64</sup> Simulation parameters such as acceleration voltage, spherical aberration (C<sub>3</sub> and C<sub>5</sub>), convergence angle, and inner/outer angle for the HAADF detector were set according to experimental conditions.

## ■ ASSOCIATED CONTENT

### ● Supporting Information

The Supporting Information is available free of charge on the ACS Publications website at DOI: 10.1021/acs.nanolett.7b01463.

Band structure calculations for monolayer and bulk ReS<sub>2</sub>, angle-dependent Raman of few-layer ReS<sub>2</sub> at 515 nm

laser excitation, 18 first-order Raman-active eigenvectors, low-frequency shear and layer breathing modes of the flakes, determination of up/down orientation and stacking of flakes, Raman spectra on the same scaling and vertical offset, Raman spectra including 785 nm laser excitation, two-dimensional plots of Figure 3, change in intensity [(%), with respect to the bulk intensity] as a function of layer thickness for different angles and laser wavelengths, and the exciton energy as a function of layer number of ReS<sub>2</sub>. It also includes corrections that were applied to the measured intensities to account for the angle dependence of the Si(100) intensity, resonant behavior of Si, and thin film interference effects in the SiO<sub>2</sub> (PDF)

## ■ AUTHOR INFORMATION

### Corresponding Authors

\*E-mail: mut11@psu.edu.

\*E-mail: angela.hightwalker@nist.gov.

### ORCID

Amber McCreary: 0000-0002-9988-5800

Yuanxi Wang: 0000-0002-0659-1134

Luis Balicas: 0000-0002-5209-0293

Angela R. Hight Walker: 0000-0003-1385-0672

### Notes

The authors declare no competing financial interest.

## ■ ACKNOWLEDGMENTS

A.M., Y.W., D.R., L.B., V.H.C., and M.T. acknowledge support by the U.S. Army Research Office MURI grant No. W911NF-11-1-0362. This research was sponsored by the Army Research Laboratory and was accomplished under Cooperative Agreement Number W911NF-16-2-0232. The views and conclusions contained in this document are those of the authors and should not be interpreted as representing the official policies, either expressed or implied, of the Army Research Laboratory or the U.S. Government. The U.S. Government is authorized to reproduce and distribute reprints for Government purposes not withstanding any copyright notation herein. Certain commercial equipment, instruments, or materials are identified in this manuscript in order to specify the experimental procedure adequately. Such identification is not intended to imply recommendation or endorsement by the National Institute of Standards and Technology, nor is it intended to imply that the materials or equipment are necessarily the best available for the purpose. Y.W. and V.H.C. acknowledge support from the National Science Foundation Materials Innovation Platform under DMR-1539916. The National High Magnetic Field Laboratory is supported by National Science Foundation Cooperative Agreement No. DMR-1157490 and the State of Florida. We are also grateful to Prof. Jia-An Yan at Towson University for insightful discussions and Dr. Gordon Shaw at NIST for atomic force microscopy measurements.

## ■ REFERENCES

- (1) Novoselov, K. S.; Geim, A. K.; Morozov, S. V.; Jiang, D.; Zhang, Y.; Dubonos, S. V.; Grigorieva, I. V.; Firsov, A. A. Electric Field Effect in Atomically Thin Carbon Films. *Science* **2004**, *306*, 666–669.
- (2) Novoselov, K. S.; Geim, A. K.; Morozov, S. V.; Jiang, D.; Katsnelson, M. I.; Grigorieva, I. V.; Dubonos, S. V.; Firsov, A. A. Two-Dimensional Gas of Massless Dirac Fermions in Graphene. *Nature* **2005**, *438*, 197–200.

- (3) Geim, A. K.; Novoselov, K. S. The Rise of Graphene. *Nat. Mater.* **2007**, *6*, 183–191.
- (4) Wang, Q. H.; Kalantar-Zadeh, K.; Kis, A.; Coleman, J. N.; Strano, M. S. Electronics and Optoelectronics of Two-Dimensional Transition Metal Dichalcogenides. *Nat. Nanotechnol.* **2012**, *7*, 699–712.
- (5) Butler, S. Z.; Hollen, S. M.; Cao, L.; Cui, Y.; Gupta, J. A.; Gutierrez, H. R.; Heinz, T. F.; Hong, S. S.; Huang, J.; Ismach, A. F.; Johnston-Halperin, E.; Kuno, M.; Plashnitsa, V. V.; Robinson, R. D.; Ruoff, R. S.; Salahuddin, S.; Shan, J.; Shi, L.; Spencer, M. G.; Terrones, M.; Windl, W.; Goldberger, J. E. Progress, Challenges, and Opportunities in Two-Dimensional Materials Beyond Graphene. *ACS Nano* **2013**, *7*, 2898–2926.
- (6) Bhimanapati, G. R.; Lin, Z.; Meunier, V.; Jung, Y.; Cha, J.; Das, S.; Xiao, D.; Son, Y.; Strano, M. S.; Cooper, V. R.; Liang, L.; Louie, S. G.; Ringe, E.; Zhou, W.; Kim, S. S.; Naik, R. R.; Sumpter, B. G.; Terrones, H.; Xia, F.; Wang, Y.; Zhu, J.; Akinwande, D.; Alem, N.; Schuller, J. A.; Schaak, R. E.; Terrones, M.; Robinson, J. A. Recent Advances in Two-Dimensional Materials beyond Graphene. *ACS Nano* **2015**, *9*, 11509–11539.
- (7) Das, S.; Robinson, J. A.; Dubey, M.; Terrones, H.; Terrones, M. Beyond Graphene: Progress in Novel Two-Dimensional Materials and van der Waals Solids. *Annu. Rev. Mater. Res.* **2015**, *45*, 1–27.
- (8) Chhowalla, M.; Shin, H. S.; Eda, G.; Li, L. J.; Loh, K. P.; Zhang, H. The Chemistry of Two-Dimensional Layered Transition Metal Dichalcogenide Nanosheets. *Nat. Chem.* **2013**, *5*, 263–275.
- (9) Lv, R.; Robinson, J. A.; Schaak, R. E.; Sun, D.; Sun, Y. F.; Mallouk, T. E.; Terrones, M. Transition Metal Dichalcogenides and Beyond: Synthesis, Properties, and Applications of Single- and Few-Layer Nanosheets. *Acc. Chem. Res.* **2015**, *48*, 56–64.
- (10) Tongay, S.; Sahin, H.; Ko, C.; Luce, A.; Fan, W.; Liu, K.; Zhou, J.; Huang, Y. S.; Ho, C. H.; Yan, J. Y.; Ogletree, D. F.; Aloni, S.; Ji, J.; Li, S. S.; Li, J. B.; Peeters, F. M.; Wu, J. Q. Monolayer Behaviour in Bulk ReS<sub>2</sub> Due to Electronic and Vibrational Decoupling. *Nat. Commun.* **2014**, *5*, 3252.
- (11) Liu, E. F.; Fu, Y. J.; Wang, Y. J.; Feng, Y. Q.; Liu, H. M.; Wan, X. G.; Zhou, W.; Wang, B. G.; Shao, L. B.; Ho, C. H.; Huang, Y. S.; Cao, Z. Y.; Wang, L. G.; Li, A. D.; Zeng, J. W.; Song, F. Q.; Wang, X. R.; Shi, Y.; Yuan, H. T.; Hwang, H. Y.; Cui, Y.; Miao, F.; Xing, D. Y. Integrated Digital Inverters Based on Two-Dimensional Anisotropic ReS<sub>2</sub> Field-Effect Transistors. *Nat. Commun.* **2015**, *6*, 6991.
- (12) Corbet, C. M.; McClellan, C.; Rai, A.; Sonde, S. S.; Tutuc, E.; Banerjee, S. K. Field Effect Transistors with Current Saturation and Voltage Gain in Ultrathin ReS<sub>2</sub>. *ACS Nano* **2015**, *9*, 363–370.
- (13) Pradhan, N. R.; McCreary, A.; Rhodes, D.; Lu, Z.; Feng, S.; Manousakis, E.; Smirnov, D.; Namburu, R.; Dubey, M.; Hight Walker, A. R.; Terrones, H.; Terrones, M.; Dobrosavljevic, V.; Balicas, L. Metal to Insulator Quantum-Phase Transition in Few-Layered ReS<sub>2</sub>. *Nano Lett.* **2015**, *15*, 8377–8384.
- (14) Aslan, O. B.; Chenet, D. A.; van der Zande, A. M.; Hone, J. C.; Heinz, T. F. Linearly Polarized Excitons in Single- and Few-Layer ReS<sub>2</sub> Crystals. *ACS Photonics* **2016**, *3*, 96–101.
- (15) Marzlik, J. V.; Kershaw, R.; Dwight, K.; Wold, A. Photoelectronic Properties of ReS<sub>2</sub> and ReSe<sub>2</sub> Single Crystals. *J. Solid State Chem.* **1984**, *51*, 170–175.
- (16) Ho, C. H.; Liao, P. C.; Huang, Y. S.; Yang, T. R.; Tiong, K. K. Optical Absorption of ReS<sub>2</sub> and ReSe<sub>2</sub> Single Crystals. *J. Appl. Phys.* **1997**, *81*, 6380–6383.
- (17) Dileep, K.; Sahu, R.; Sarkar, S.; Peter, S. C.; Datta, R. Layer specific optical band gap measurement at nanoscale in MoS<sub>2</sub> and ReS<sub>2</sub> van der Waals compounds by high resolution electron energy loss spectroscopy. *J. Appl. Phys.* **2016**, *119*, 114309.
- (18) Cakir, D.; Sahin, H.; Peeters, F. M. Doping of Rhenium Disulfide Monolayers: a Systematic First Principles Study. *Phys. Chem. Chem. Phys.* **2014**, *16*, 16771–16779.
- (19) Yu, Z. G.; Cai, Y.; Zhang, Y.-W. Robust Direct Bandgap Characteristics of One- and Two-Dimensional ReS<sub>2</sub>. *Sci. Rep.* **2015**, *5*, 13783.
- (20) Zhong, H. X.; Gao, S. Y.; Shi, J. J.; Yang, L. Quasiparticle Band Gaps, Excitonic effects, and Anisotropic Optical Properties of the Monolayer Distorted 1T Diamond-Chain Structures ReS<sub>2</sub> and ReSe<sub>2</sub>. *Phys. Rev. B: Condens. Matter Mater. Phys.* **2015**, *92*, 115438.
- (21) Lin, Y.-C.; Komsa, H.-P.; Yeh, C.-H.; Bjorkman, T.; Liang, Z.-Y.; Ho, C.-H.; Huang, Y.-S.; Chiu, P.-W.; Krasheninnikov, A. V.; Suenaga, K. Single-Layer ReS<sub>2</sub>: Two-Dimensional Semiconductor with Tunable In-Plane Anisotropy. *ACS Nano* **2015**, *9*, 11249–11257.
- (22) Liu, E. F.; Long, M. S.; Zeng, J. W.; Luo, W.; Wang, Y. J.; Pan, Y. M.; Zhou, W.; Wang, B. G.; Hu, W. D.; Ni, Z. H.; You, Y. M.; Zhang, X. A.; Qin, S. Q.; Shi, Y.; Watanabe, K.; Taniguchi, T.; Yuan, H. T.; Hwang, H. Y.; Cui, Y.; Miao, F.; Xing, D. Y. High Responsivity Phototransistors Based on Few-Layer ReS<sub>2</sub> for Weak Signal Detection. *Adv. Funct. Mater.* **2016**, *26*, 1938–1944.
- (23) Shim, J.; Oh, A.; Kang, D. H.; Oh, S.; Jang, S. K.; Jeon, J.; Jeon, M. H.; Kim, M.; Choi, C.; Lee, J.; Lee, S.; Yeom, G. Y.; Song, Y. J.; Park, J. H. High-Performance 2D Rhenium Disulfide (ReS<sub>2</sub>) Transistors and Photodetectors by Oxygen Plasma Treatment. *Adv. Mater.* **2016**, *28*, 6985–6992.
- (24) Chenet, D. A.; Aslan, O. B.; Huang, P. Y.; Fan, C.; van der Zande, A. M.; Heinz, T. F.; Hone, J. C. In-Plane Anisotropy in Mono- and Few-Layer ReS<sub>2</sub> Probed by Raman Spectroscopy and Scanning Transmission Electron Microscopy. *Nano Lett.* **2015**, *15*, S667–S672.
- (25) Nagler, P.; Plechinger, G.; Schueller, C.; Korn, T. Observation of Anisotropic Interlayer Raman Modes in Few-Layer ReS<sub>2</sub>. *Phys. Status Solidi RRL* **2016**, *10*, 185–189.
- (26) Mao, N. N.; Tang, J. Y.; Xie, L. M.; Wu, J. X.; Han, B. W.; Lin, J. J.; Deng, S. B.; Ji, W.; Xu, H.; Liu, K. H.; Tong, L. M.; Zhang, J. Optical Anisotropy of Black Phosphorus in the Visible Regime. *J. Am. Chem. Soc.* **2016**, *138*, 300–305.
- (27) Yang, S. X.; Wang, C.; Sahin, H.; Chen, H.; Li, Y.; Li, S. S.; Suslu, A.; Peeters, F. M.; Liu, Q.; Li, J. B.; Tongay, S. Tuning the Optical, Magnetic, and Electrical Properties of ReSe<sub>2</sub> by Nanoscale Strain Engineering. *Nano Lett.* **2015**, *15*, 1660–1666.
- (28) Yang, S. X.; Tongay, S.; Yue, Q.; Li, Y. T.; Li, B.; Lu, F. Y. High-Performance Few-layer Mo-doped ReSe<sub>2</sub> Nanosheet Photodetectors. *Sci. Rep.* **2015**, *4*, 5442.
- (29) Liu, F. C.; Zheng, S. J.; He, X. X.; Chaturvedi, A.; He, J. F.; Chow, W. L.; Mion, T. R.; Wang, X. L.; Zhou, J. D.; Fu, Q. D.; Fan, H. J.; Tay, B. K.; Song, L.; He, R. H.; Kloc, C.; Ajayan, P. M.; Liu, Z. Highly Sensitive Detection of Polarized Light Using Anisotropic 2D ReS<sub>2</sub>. *Adv. Funct. Mater.* **2016**, *26*, 1169–1177.
- (30) Wolverson, D.; Crampin, S.; Kazemi, A. S.; Ilie, A.; Bending, S. J. Raman Spectra of Monolayer, Few-Layer, and Bulk ReSe<sub>2</sub>: An Anisotropic Layered Semiconductor. *ACS Nano* **2014**, *8*, 11154–11164.
- (31) Castellanos-Gomez, A.; Vicarelli, L.; Prada, E.; Island, J. O.; Narasimha-Acharya, K. L.; Blanter, S. I.; Groenendijk, D. J.; Buscema, M.; Steele, G. A.; Alvarez, J. V. Isolation and Characterization of Few-Layer Black Phosphorus. *2D Mater.* **2014**, *1*, 025001.
- (32) Carvalho, B. R.; Malard, L. M.; Alves, J. M.; Fantini, C.; Pimenta, M. A. Symmetry-Dependent Exciton-Phonon Coupling in 2D and Bulk MoS<sub>2</sub> Observed by Resonance Raman Scattering. *Phys. Rev. Lett.* **2015**, *114*, 136403.
- (33) Berkdemir, A.; Gutierrez, H. R.; Botello-Mendez, A. R.; Perea-Lopez, N.; Elias, A. L.; Chia, C.-I.; Wang, B.; Crespi, V. H.; Lopez-Urias, F.; Charlier, J.-C.; Terrones, H.; Terrones, M. Identification of Individual and Few Layers of WS<sub>2</sub> Using Raman Spectroscopy. *Sci. Rep.* **2013**, *3*, 1755.
- (34) Golasa, K.; Grzeszczyk, M.; Leszczynski, P.; Faugeras, C.; Nicolet, A. A. L.; Wymolek, A.; Potemski, M.; Babinski, A. Multiphonon Resonant Raman Scattering in MoS<sub>2</sub>. *Appl. Phys. Lett.* **2014**, *104*, 092106.
- (35) Golasa, K.; Grzeszczyk, M.; Bozek, R.; Leszczynski, P.; Wymolek, A.; Potemski, M.; Babinski, A. Resonant Raman Scattering in MoS<sub>2</sub> - From Bulk to Monolayer. *Solid State Commun.* **2014**, *197*, 53–56.
- (36) Lee, J. U.; Kim, K.; Cheong, H. Resonant Raman and Photoluminescence Spectra of Suspended Molybdenum Disulfide. *2D Mater.* **2015**, *2*, 044003.

- (37) del Corro, E.; Botello-Mendez, A.; Gillet, Y.; Elias, A. L.; Terrones, H.; Feng, S.; Fantini, C.; Rhodes, D.; Pradhan, N.; Balicas, L.; Gonze, X.; Charlier, J. C.; Terrones, M.; Pimenta, M. A. Atypical Exciton-Phonon Interactions in WS<sub>2</sub> and WSe<sub>2</sub> Monolayers Revealed by Resonance Raman Spectroscopy. *Nano Lett.* **2016**, *16*, 2363–2368.
- (38) Carvalho, B. R.; Wang, Y.; Mignuzzi, S.; Roy, D.; Terrones, M.; Fantini, C.; Crespi, V. H.; Malard, L. M.; Pimenta, M. A. Intervalley Scattering by Acoustic Phonons in Two-Dimensional MoS<sub>2</sub> Revealed by Double-Resonance Raman Spectroscopy. *Nat. Commun.* **2017**, *8*, 14670.
- (39) Lee, C.; Yan, H.; Brus, L. E.; Heinz, T. F.; Hone, J.; Ryu, S. Anomalous Lattice Vibrations of Single- and Few-Layer MoS<sub>2</sub>. *ACS Nano* **2010**, *4*, 2695–2700.
- (40) Feng, Y. Q.; Zhou, W.; Wang, Y. J.; Zhou, J.; Liu, E. F.; Fu, Y. J.; Ni, Z. H.; Wu, X. L.; Yuan, H. T.; Miao, F.; Wang, B. G.; Wan, X. G.; Xing, D. Y. Raman Vibrational Spectra of Bulk to Monolayer ReS<sub>2</sub> with Lower Symmetry. *Phys. Rev. B: Condens. Matter Mater. Phys.* **2015**, *92*, 054110.
- (41) Zhao, H.; Wu, J.; Zhong, H.; Guo, Q.; Wang, X.; Xia, F.; Yang, L.; Tan, P.; Wang, H. Interlayer Interactions in Anisotropic Atomically Thin Rhenium Diselenide. *Nano Res.* **2015**, *8*, 3651–3661.
- (42) Lorchat, E.; Froehlicher, G.; Berciaud, S. Splitting of Interlayer Shear Modes and Photon Energy Dependent Anisotropic Raman Response in *N*-Layer ReSe<sub>2</sub> and ReS<sub>2</sub>. *ACS Nano* **2016**, *10*, 2752–2760.
- (43) Hart, L.; Dale, S.; Hoye, S.; Webb, J. L.; Wolverson, D. Rhenium Dichalcogenides: Layered Semiconductors with Two Vertical Orientations. *Nano Lett.* **2016**, *16*, 1381–1386.
- (44) He, R.; Yan, J. A.; Yin, Z. Y.; Ye, Z. P.; Ye, G. H.; Cheng, J.; Li, J.; Lui, C. H. Coupling and Stacking Order of ReS<sub>2</sub> Atomic Layers Revealed by Ultralow-Frequency Raman Spectroscopy. *Nano Lett.* **2016**, *16*, 1404–1409.
- (45) Qiao, X.-F.; Wu, J.-B.; Zhou, L.; Qiao, J.; Shi, W.; Chen, T.; Zhang, X.; Zhang, J.; Ji, W.; Tan, P.-H. Polytypism and Unexpected Strong Interlayer Coupling in Two-Dimensional Layered ReS<sub>2</sub>. *Nanoscale* **2016**, *8*, 8324–8332.
- (46) DeWolf, I. Micro-Raman Spectroscopy to Study Local Mechanical Stress in Silicon Integrated Circuits. *Semicond. Sci. Technol.* **1996**, *11*, 139–154.
- (47) Renucci, J. B.; Tyte, R. N.; Cardona, M. Resonant Raman-Scattering in Silicon. *Phys. Rev. B* **1975**, *11*, 3885–3895.
- (48) Yoon, D.; Moon, H.; Son, Y. W.; Choi, J. S.; Park, B. H.; Cha, Y. H.; Kim, Y. D.; Cheong, H. Interference Effect on Raman Spectrum of Graphene on SiO<sub>2</sub>/Si. *Phys. Rev. B: Condens. Matter Mater. Phys.* **2009**, *80*, 125422.
- (49) Zhang, H.; Wan, Y.; Ma, Y. G.; Wang, W.; Wang, Y. L.; Dai, L. Interference Effect on Optical Signals of Monolayer MoS<sub>2</sub>. *Appl. Phys. Lett.* **2015**, *107*, 101904.
- (50) Li, S.-L.; Miyazaki, H.; Song, H.; Kuramochi, H.; Nakaharai, S.; Tsukagoshi, K. Quantitative Raman Spectrum and Reliable Thickness Identification for Atomic Layers on Insulating Substrates. *ACS Nano* **2012**, *6*, 7381–7388.
- (51) Soubelet, P.; Bruchhausen, A. E.; Fainstein, A.; Nogajewski, K.; Faugeras, C. Resonance Effects in the Raman Scattering of Monolayer and Few-Layer MoSe<sub>2</sub>. *Phys. Rev. B: Condens. Matter Mater. Phys.* **2016**, *93*, 155407.
- (52) Gillet, Y.; Giantomassi, M.; Gonze, X. First-Principles Study of Excitonic Effects in Raman Intensities. *Phys. Rev. B: Condens. Matter Mater. Phys.* **2013**, *88*, 094035.
- (53) Guo, H. H.; Yang, T.; Yamamoto, M.; Zhou, L.; Ishikawa, R.; Ueno, K.; Tsukagoshi, K.; Zhang, Z. D.; Dresselhaus, M. S.; Saito, R. Double Resonance Raman Modes in Monolayer and Few-Layer MoTe<sub>2</sub>. *Phys. Rev. B: Condens. Matter Mater. Phys.* **2015**, *91*, 205415.
- (54) Terrones, H.; Del Corro, E.; Feng, S.; Poumirol, J. M.; Rhodes, D.; Smirnov, D.; Pradhan, N. R.; Lin, Z.; Nguyen, M. A. T.; Elias, A. L.; Mallouk, T. E.; Balicas, L.; Pimenta, M. A.; Terrones, M. New First Order Raman-active Modes in Few Layered Transition Metal Dichalcogenides. *Sci. Rep.* **2015**, *4*, 4215.
- (55) Novoselov, K. S.; Jiang, D.; Schedin, F.; Booth, T. J.; Khotkevich, V. V.; Morozov, S. V.; Geim, A. K. Two-Dimensional Atomic Crystals. *Proc. Natl. Acad. Sci. U. S. A.* **2005**, *102*, 10451–10453.
- (56) Lu, X.; Luo, X.; Zhang, J.; Quek, S. Y.; Xiong, Q. H. Lattice Vibrations and Raman Scattering in Two-Dimensional Layered Materials Beyond Graphene. *Nano Res.* **2016**, *9*, 3559–3597.
- (57) Martin, R. M.; Falicov, L. M. In *Light Scattering in Solids I*; Cardona, M., Ed.; Springer: Berlin, 1983; Vol. 8, p 79.
- (58) Giannozzi, P.; Baroni, S.; Bonini, N.; Calandra, M.; Car, R.; Cavazzoni, C.; Ceresoli, D.; Chiarotti, G. L.; Cococcioni, M.; Dabo, I. QUANTUM ESPRESSO: A Modular and Open-Source Software Project for Quantum Simulations of Materials. *J. Phys. Cond. Matter* **2009**, *21*, 395502.
- (59) Grimme, S. Semiempirical GGA-Type Density Functional Constructed with a Long-Range Dispersion Correction. *J. Comput. Chem.* **2006**, *27*, 1787–1799.
- (60) Komsa, H.-P.; Krashenninnikov, A. Electronic Structures and Optical Properties of Realistic Transition Metal Dichalcogenide Heterostructures From First Principles. *Phys. Rev. B: Condens. Matter Mater. Phys.* **2013**, *88*, 085318.
- (61) Kresse, G.; Furthmüller, J. Efficient Iterative Schemes for *ab initio* Total Energy Calculations Using a Plane-Wave Basis Set. *Phys. Rev. B: Condens. Matter Mater. Phys.* **1996**, *54*, 11169.
- (62) Kresse, G.; Furthmüller, J. Efficiency of *ab initio* Total Energy Calculations for Metals and Semiconductors Using a Plane-Wave Basis Set. *Comput. Mater. Sci.* **1996**, *6*, 15–50.
- (63) Elias, A. L.; Perea-Lopez, N.; Castro-Beltran, A.; Berkdemir, A.; Lv, R. T.; Feng, S. M.; Long, A. D.; Hayashi, T.; Kim, Y. A.; Endo, M.; Gutierrez, H. R.; Pradhan, N. R.; Balicas, L.; Houk, T. E. M.; Lopez-Urias, F.; Terrones, H.; Terrones, M. Controlled Synthesis and Transfer of Large-Area WS<sub>2</sub> Sheets: From Single Layer to Few Layers. *ACS Nano* **2013**, *7*, 5235–5242.
- (64) Koch, C. T. Determination of Core Structure Periodicity and Point Defect Density Along Dislocations. Ph.D. Thesis, Arizona State University, Tempe, AZ, 2002.